

Article

TiO₂-Doped Chitosan Microspheres Supported on Cellulose Acetate Fibers for Adsorption and Photocatalytic Degradation of Methyl Orange

Xuejuan Shi ¹, Xiaoxiao Zhang ¹, Liang Ma ¹, Chunhui Xiang ²  and Lili Li ^{1,*} 

¹ Key Laboratory of Automobile Materials, Ministry of Education, and College of Materials Science and Engineering, Jilin University, Changchun 130022, China

² Department of Apparel, Events and Hospitality Management, 31 MacKay Hall, Iowa State University, Ames, IA 50011, USA

* Correspondence: lilylee@jlu.edu.cn; Tel.: +86-0431-8509-5170

Received: 26 June 2019; Accepted: 12 July 2019; Published: 2 August 2019



Abstract: Chitosan/cellulose acetate (CS/CA) used as a biopolymer systema, with the addition of TiO₂ as photocatalyst (C-T/CA) were fabricated by alternating electrospinning/electrospraying technology. The uniform dispersion of TiO₂ and its recovery after the removal of methyl orange (MO) was achieved by incorporating TiO₂ in CS electrospayed hemispheres. The effects of pH values, contact time, and the amount of TiO₂ on adsorption and photocatalytic degradation for MO of the C-T/CA were investigated in detail. When TiO₂ content was 3 wt %, the highest MO removal amount for fiber membranes (C-T-3/CA) reached 98% at pH value 4 and MO concentration of 40 mg/L. According to the data analysis, the pseudo-second-order kinetic and Freundlich isotherm model were well fitted to kinetic and equilibrium data of MO removal. Especially for C-T-3/CA, the fiber membrane exhibited multiple layers of adsorption. All these results indicated that adsorption caused by electrostatic interaction and photocatalytic degradation were involved in the MO removal process. This work provides a potential method for developing a novel photocatalyst with excellent catalytic activity, adsorbing capability and recycling use.

Keywords: TiO₂; chitosan; electrospinning; electrospraying; methyl orange; photocatalytic degradation

1. Introduction

With the quick progress of industrial technology, water pollution generated from organic dye contaminants has become an increasing global environmental concern in recent years [1–4]. Organic dyes are mainly generated from manufacturing, such as textile finishing, plastics, paper, cosmetics, pharmaceuticals and food processing. It can cause serious problems for both the environment and to human beings [5–10]. Up until now, several methods such as chemical oxidation, coagulation, adsorption, biodegradation, photocatalysis, and reverse osmosis, have been developed to treat dye contaminated wastewater [11–14]. Particularly, photocatalysis is considered a “green” treatment method which uses solar energy effectively for the degradation of organic pollutants [15–19]. Adsorption is also considered a valid method for the removal of dye in aqueous solutions with high efficiency, low price and easy operation [20–22].

At present, researchers have found that the combination of adsorption and photocatalysis had excellent potential applications for dye treatment [23]. TiO₂ is a type of common semiconductor photocatalyst on account of its prominent characteristics of chemical resistance, excellent catalytic activity, mechanical robustness, and low cost [24–28]. While the low dispersibility, inconvenient recovery, low adsorption performance of TiO₂ limit its use in photocatalysis applications [29]. Absorbent

materials with good adsorption performance on organic pollutants are often used as carrier materials to improve the photocatalysis capability of TiO₂.

Ideal carrier materials should provide stable anchoring of TiO₂, outstanding structure stability, selective adsorption for target dye pollutions and the transfer of organic dye molecules to the vicinity of the photocatalytic site. Multifarious materials have been developed for photocatalytic degradation carrier materials, comprising silica, ceramic, polymers, activated carbon, zeolite, and glass. As an environmentally friendly, nontoxic, biodegradable, biocompatible natural macromolecule [30–34], CS with functional groups of hydroxyl and amino groups derived from deacetylation of polysaccharide chitin, is a promising carrier material [35–38]. Li et al. produced pure CS membranes by electrospinning, exhibiting high adsorption capacity for acid blue-113 [37]. Huang et al. produced an organoclay/CS hybrid system, allowing efficient and concurrent adsorption of different dyes [38]. However, CS is easily soluble in water when amino groups are protonated, making it difficult to maintain integrity of the whole materials. As a hydrophilic, environmentally friendly, biodegradable, and renewable material [39–43], CA has characteristics of non-specific adsorption, and its hydroxyl and ester groups can form stable hydrogen bonding with certain polar functional groups [44,45]. Electrospinning technology is a common and effective method for the preparation of adsorbents [14]. Doh et al. electrospun TiO₂ nanofibers had a higher degradation rate of organic dye than TiO₂ nanoparticles because of a high specific surface area and excellent dispersibility [4]. Razzaz et al. proved that CS/TiO₂ electrospun membranes had higher effective surface area, structural stability and adsorption capacity for metal ions compared with TiO₂-coated CS nanofibers [46].

In this study, based on CA electrospun fibers, C-T/CA fiber membranes were successfully prepared via electrospaying CS/TiO₂ concave hemispheres on the surface of CA fibers. As a substrate material, CA was expected to improve the water flux of fiber membranes effectively so that aqueous solutions of organic pollutant, MO could rapidly penetrate into the interior of membranes. The CS hemispheres might disperse TiO₂ nanoparticles, have good adsorption performance of MO, and transfer MO to the vicinity of TiO₂ active sites for further photocatalytic degradation. The morphology of fiber membranes were characterized by SEM. Effects of TiO₂ content, pH values, contact time at different MO concentration for adsorption and photocatalytic degradation of MO were investigated. The MO removal mechanism was surveyed by FTIR, XPS and BET.

2. Experiment

2.1. Materials

CS (90% deacetylated, average M_w = 200,000 Da), TiO₂ nanoparticles (anatase-type nanopowder, particle size < 25 nm, metal basis), CA (white powder, M_n ≈ 30,000 Da, acetyl content ≈ 39.7 wt %, DS = 2.45) and MO were all purchased from Aladdin Industrial Corporation, Shanghai, China. Acetic acid (HAc) and acetone were purchased from Beijing Chemical Works, Beijing, China. Deionized water was obtained from the laboratory. The chemicals were all of analytical grade and used without further purification.

2.2. Preparation of Polymer Solutions

10 wt % CA (*w/w*) was dissolved in acetone/deionized water (85/15, *w/w*) and 2 wt % CS (*w/w*) was dissolved in 90% acetic acid (*v/v*), respectively. The solutions were stirred for 24 h at room temperature to obtain the uniform solutions. Then, the various contents of TiO₂ (1%, 2%, 3%, 4%, 5%, *w/w*) were added to CS solutions at room temperature and stirred for 24 h. The C-T-X solutions were obtained, where X stands for the content of TiO₂ (1, 2, 3, 4, 5 wt %). The solutions were placed in an ultrasonic water bath for 30 min before using. The frequency of ultrasonication was 25 kHz.

2.3. Fabrication of C-T/CA Fiber Membranes

The fabrication processes including (I) electrospinning and (II) electrospraying are shown in Figure 1. The solution was loaded into a 5 mL plastic syringe. The electrospinning conditions included the applied voltage of 20 kV, the 15 cm distance between the tip of the needle and the collector, and the flow rate of 1.0 mL/h. The condition for electrospraying was 18 kV voltage with a distance of 15 cm between the tip of the needle and the collector, and the flow rate was 0.3 mL/h. Then the membrane was dried at 25 °C for 24 h, and peeled off aluminum foil for further study.

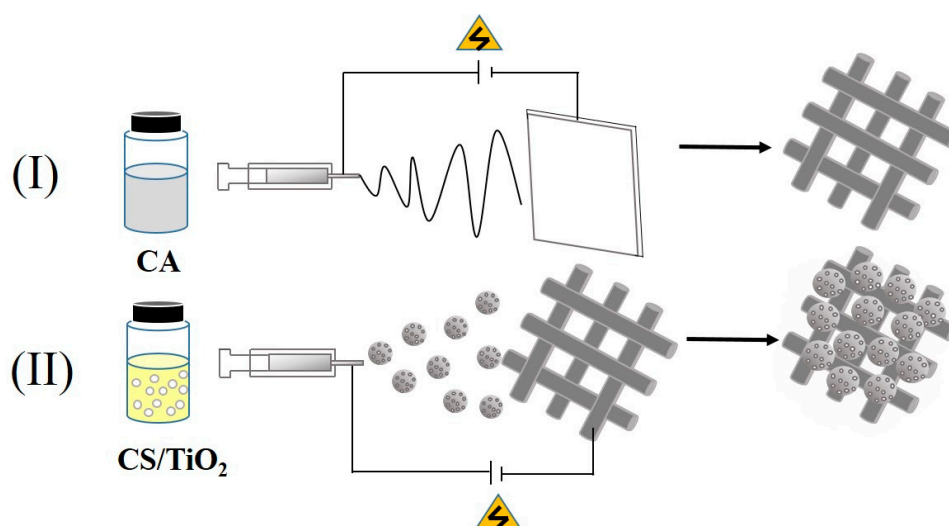


Figure 1. The preparation of C-T/CA fiber membranes: (I) Electrospinning, and (II) electrospraying.

2.4. Characterizations

The viscosity of precursor solutions was measured by a viscosimeter (NDJ-1, Yutong, Shanghai, China). The electrical conductivity of the solutions was measured using a conductometer (DDS-11A, Shengci, Shanghai, China). All measurements were taken 3 times at room temperature. The morphology and structure of membranes were characterized by SEM (JSM-6700F, JEOL, Tokyo, Japan). All samples were sputtered with platinum under vacuum before assessment. The average microspheres diameters were measured by Image J software. Surface area, pore volume and pore size were characterized by N₂ adsorption and desorption using a Brunauer–Emmett–Teller analyzer (BET, Autosorb-iQ2, Quantachrome Instruments, Shanghai, China). The structures of the composite fibers were analyzed by FTIR spectroscopy (FTIR-4100, Jasco, Shanghai, China), within the wavenumber ranging from 400 to 4000 cm⁻¹ and a wide angle X-ray diffractometer (XRD, D/Max, Rigaku, Beijing, China), under mode of 40 kV and 50 mA, $\lambda = 1.5406 \text{ \AA}$ radiation using copper-K alpha. The samples were scanned in the 2 θ range from 5° to 60° with a scanning rate of 30 min⁻¹. The chemical composition of membrane surfaces were analyzed by XPS (ESCALab220i-XL, VG Scientific, Waltham, MA, USA) with Al K α X-ray source, Ni-filtered radiation, 40 kV of tube electric pressure and 30 mA of tube electric current.

2.5. Investigations on MO Adsorption and Photocatalysis Study

Organic dye MO was used as the adsorbate for adsorption and photocatalysis studies of fiber mats. 20 mg of fiber mats were immersed in 40 mg/L MO aqueous solution (20 mL). The solution with fiber mats was stirred in dark conditions for 1 h to reach the adsorption equilibrium. After that, the mix solution was irradiated for 30 min in a photodegradation reactor under UV light (wavelength of 365 nm) by mercury lamp (25 W). The mixed solution (6 mL) was taken out every 5 min and centrifuged. The centrifugation was used to separate the solid particles in the suspension from the liquid to obtain a supernatant for subsequent absorbance detection. The UV spectrophotometer of the residual MO content was recorded. The process was repeated six times. The other set of photocatalytic experiments

were performed under visible light (wavelength of 600 nm) using a 350 W xenon lamp. The operation was the same as the process using UV light. The concentration of the residual MO was recorded every 20 min for 120 min. The adsorption and photocatalytic degradation R (%) of membranes to MO was calculated by the Equation (1):

$$R(\%) = \frac{A_0 - A_t}{A_0} \times 100\% \quad (1)$$

where A_0 and A_t are the original and equilibrium absorbances of the MO solutions.

The batch experiments of MO onto the fiber membranes were carried out as functions of TiO_2 concentration (0–5 wt %), pH (4–9), contact time (0–85 min), and initial concentration (10–80 mg/L) at room temperature. The adsorption and photocatalysis ability was computed as follows:

$$q_t = \frac{C_0 - C_t}{m} \times V \quad (2)$$

where q_t (mg/g) represented the removal amount at time t , C_0 (mg/L) and C_t (mg/L) are the original and equilibrium concentrations of the MO solutions, V (L) is the volume of MO solutions, m (g) is the quantity of fiber membrane.

In the reusability experiment, the used adsorbent was washed by deionized water. Then the supernatant of the solution, after the reaction was replaced by fresh MO solution. The photodegradation reaction was carried out under UV illumination with magnetic stirring for 1 h. This experiment was cycled five times.

3. Results and Discussion

3.1. Morphology Observation

The morphology and diameter distributions of the CA substrate are displayed in Figure 2. The surfaces of the CA fibers were smooth without beads. The mean diameter of CA fibers was $0.55 \pm 0.24 \mu\text{m}$ (shown in Figure 2b).

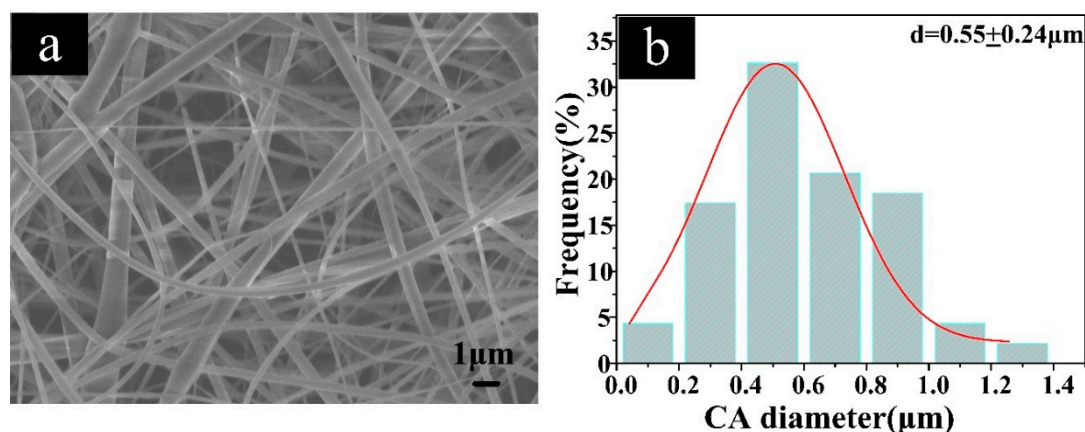


Figure 2. (a) The morphology, and (b) the diameter distribution of the CA fibers.

The morphology and the diameter distributions of the CS microspheres with different additions of TiO_2 are shown in Figure 3. Pure CS showed concave hemisphere morphology as shown in Figure 3a. With the content of 1, 2, 3 wt % TiO_2 , CS still maintained the concave hemisphere morphology, and TiO_2 nanoparticles were evenly distributed on the surface of CS hemispheres (see Figure 3b–d). When TiO_2 content was 4 wt % and 5 wt %, TiO_2 nanoparticles begun to accumulate, and the original uniform morphology of CS hemispheres gradually disappeared (Figure 2e,f).

The particle size of pure CS hemispheres was $1.07 \pm 0.24 \mu\text{m}$. With the increase of TiO_2 content from 1 wt % to 3 wt % (Figure 3b₁–d₁), the diameters of CS hemispheres were $1.35 \pm 0.26 \mu\text{m}$,

1.40 ± 0.28 μm and 1.46 ± 0.34 μm, showing an upward trend. This was because the increase of viscosity was more important than the conductivity of the electrospayed solution (Table 1). As the content of TiO₂ continued to increase, the diameters of CS hemispheres were 1.10 ± 0.24 μm and 1.11 ± 0.30 μm, respectively. The quick increase in the viscosity of the solutions led to the agglomeration of TiO₂ on the surface of CS hemispheres, as shown in Figure 3e₁,f₁. The size of the decrease in the CS hemispheres was due to an increase in the conductivity of the electrospay solution.

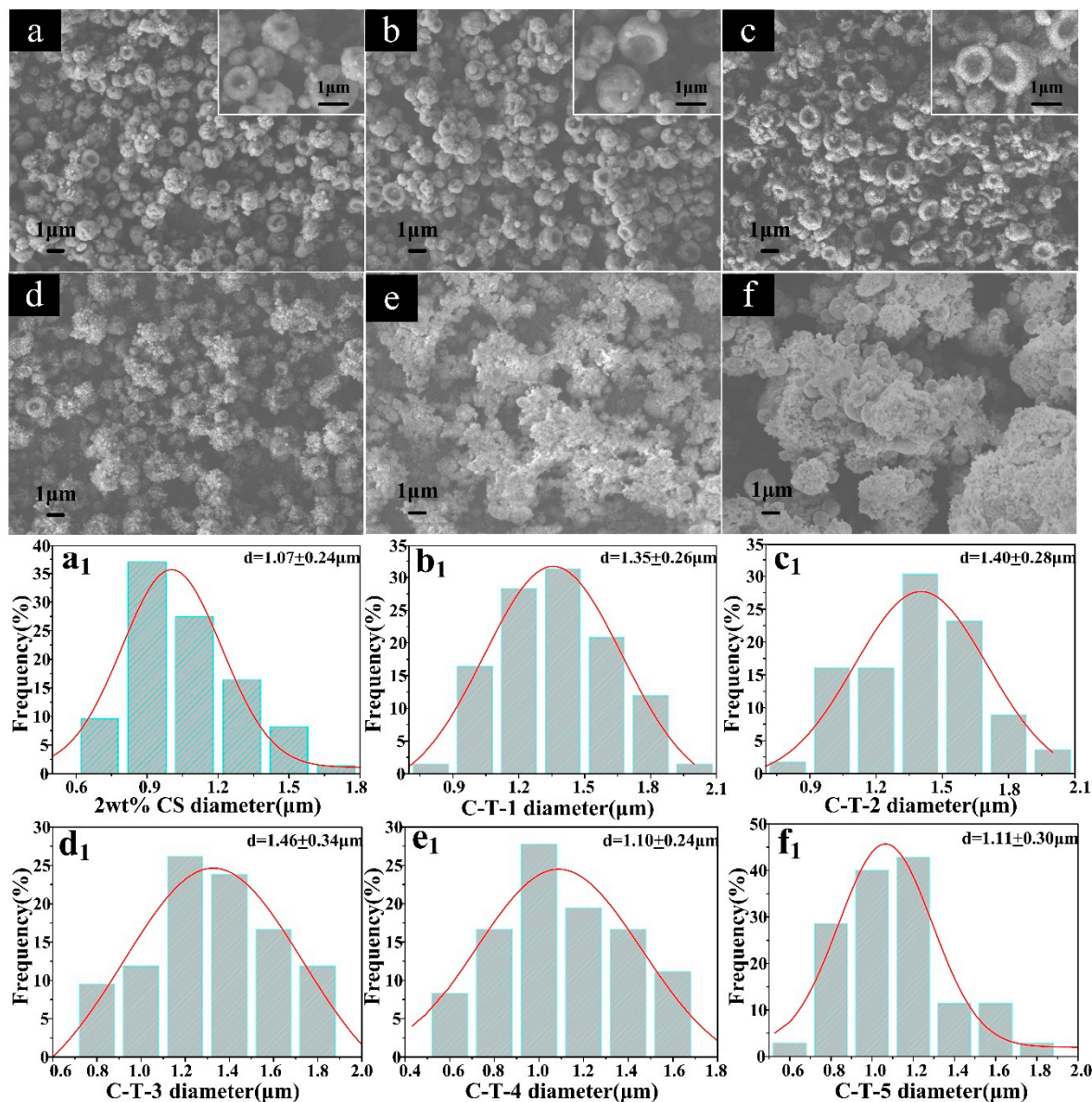


Figure 3. SEM images and diameter distributions of the microspheres. (a) and (a₁) 2 wt % CS, (b) and (b₁) C-T-1, (c) and (c₁) C-T-2, (d) and (d₁) C-T-3, (e) and (e₁) C-T-4, (f) and (f₁) C-T-5.

Table 1. The parameters of C-T-X electrospaying solutions.

TiO ₂ Content	0%	1%	2%	3%	4%	5%
Viscosity (mPa s)	140.7	158.8	172.5	183.6	209.5	220.4
Conductivity (μS cm ⁻¹)	219.0	230.7	243.8	256.1	265.0	273.4

3.2. XRD Characterization

The XRD patterns of all the samples are illuminated in Figure 4. The broad peak at 20.10° and 22.01° were characteristic peaks of CS and CA, respectively [47,48]. TiO_2 powder showed three sharp feature peaks at 48.06° , 37.86° and 25.41° of 2θ values [45]. Compared with XRD of CA powders, the peak at 22.01° of CS/CA was weakened due to the addition of amorphous CS which inhibited crystallization of CA. Compared with XRD of CS and CA powders, the peaks at 20.10° and 22.01° of C-T-3/CA were weakened due to the addition of TiO_2 which inhibited crystallization of CS and CA. It indicated that there were interactions between TiO_2 and CS/CA, which might stabilize TiO_2 on the membranes [45].

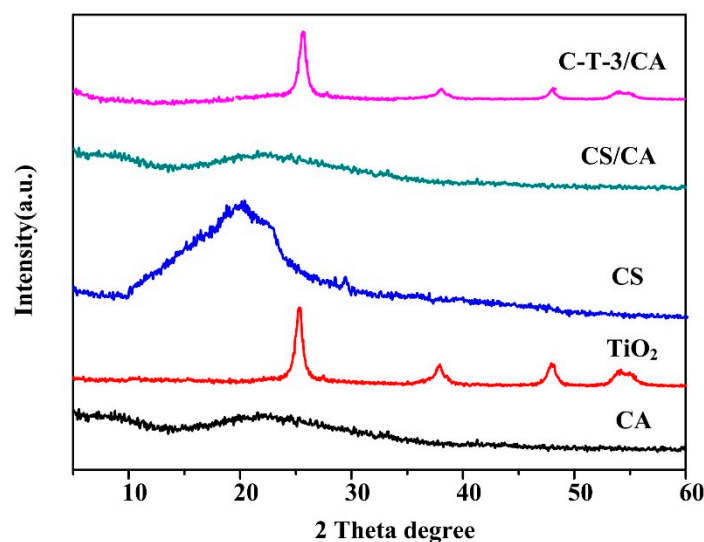


Figure 4. XRD spectra of CA, TiO_2 , CS powders, CS/CA and C-T-3/CA fiber membranes.

3.3. MO Removal Analysis

3.3.1. Effect of TiO_2 Content on MO Removal

The effect of the amount of TiO_2 on the removal of MO under visible light is demonstrated in Figure 5. Before visible light irradiation, the absorbance of MO solutions for all samples decreased due to adsorption of MO by the CS based membrane. Under visible light, the absorbance of all solutions with different fibrous membranes decreased as the reaction time increased (shown in Figure 5a). There was a significantly faster removal trend for the MO in visible light than in darkness because of the effects of both adsorption and photocatalysis. The removal of MO consisted of two stages for all samples. In the first stage, as the reaction time increased, the removal rate of MO was fast. In the second stage, the removal rate declined and got close to an equilibrium state. All samples could reach saturation state at 120 min. In combination with Figure 5b, the removal amount increased at first and then decreased with a further increase of TiO_2 content. When the TiO_2 content was higher than 3 wt %, the MO removal amount declined. This might be attributed to the reduction of the reaction sites by the TiO_2 agglomeration. Therefore, the best adsorption and photocatalysis performance was obtained at 3 wt % content of TiO_2 for CS based adsorbents.

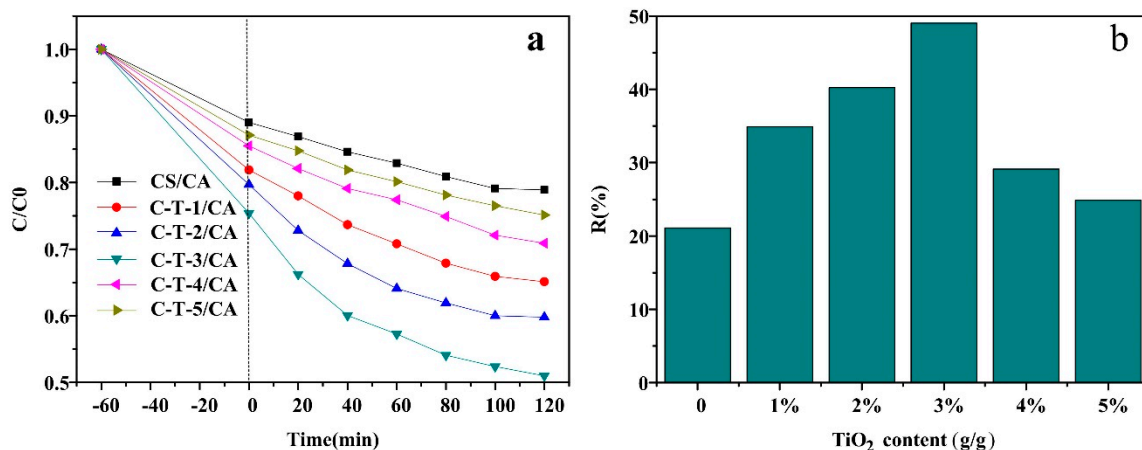


Figure 5. MO removal performance under visible light. (a) The effect of reaction time on absorption amount, (b) the effect TiO_2 content on removal rate.

The effect of TiO_2 contents on the MO removal under UV light is demonstrated in Figure 6. Under UV light, the absorbance of all solutions decreased faster than samples in darkness because of concurrent adsorption and photocatalytic degradation as the reaction time increased (shown in Figure 6a). A similar situation was found as in the visible light, where the removal of MO consisted of two stages for all samples. In the first stage, the removal rate of MO was fast as reaction time increased. In the second stage, the removal rate declined and then got close to an equilibrium state. All samples could reach saturation state at 30 min [20]. In Figure 6b, it can be seen that the removal amount increased at first and then decreased with further increase of TiO_2 content. When the TiO_2 content was higher than 3 wt %, the MO removal amount declined. This might be attributed to the reduction of the reaction sites by the TiO_2 agglomeration. The removal amount of MO by adsorption and photocatalytic degradation under UV light were superior to that in visible light because of more energy for electronic transitions [23]. Therefore, C-T-3/CA was selected for further MO removal studies by UV irradiation in the following tests.

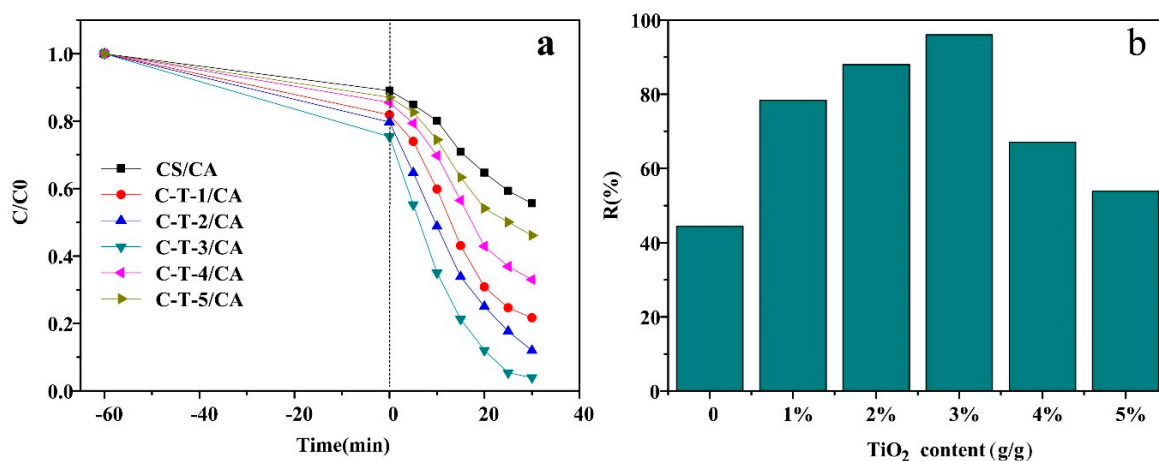


Figure 6. MO removal performance under UV light. (a) The effect of reaction time on absorption amount. (b) The effect of TiO_2 content on removal rate.

3.3.2. Effect of pH Values on the MO Removal

The pH value, as a crucial parameter, controlled the MO removal ability by affecting the degree of ionization of hydrogen ions, hydroxide ions in solutions and structural stability. Figure 7 shows the removal amount of MO in the pH value range from 4 to 9 under UV light. Both samples exhibited high removal amount with pH value in the range of 4–6, and MO removal amount gradually declined as the pH value increased. C-T-3/CA had a higher removal amount than CS/CA due to both adsorption and photocatalysis for C-T-3/CA. The removal amount was greatly improved by the addition of TiO₂ (that allowed for simultaneous adsorption and photocatalysis) under acidic conditions. This was because under acidic conditions, the –NH₂ on the CS molecule was protonated, and TiO₂ existed in the form of TiOH₂⁺, resulting in the electrostatic attraction among –SO₃[−] in MO, –NH₃⁺ and TiOH₂⁺ [48,49]. Under alkaline conditions, the –NH₂ on the CS molecule was deprotonated, TiO₂ generated the TiO[−], and an electrostatic repulsion appeared between fibrous membranes and MO, which resulted in the decrease of removal amount [47]. The maximum removal amount of MO for both samples was obtained at pH = 4.

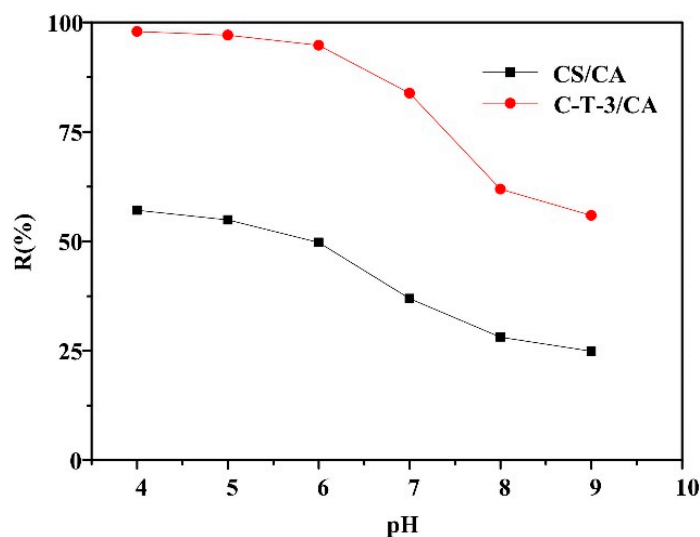


Figure 7. Effect of pH values on the MO removal amount (initial concentration 40 mg/L).

3.3.3. Effect of Initial MO Concentration on the MO Removal

The effect of initial MO concentration on MO removal is indicated in Figure 8. The MO removal ratio of CS/CA and C-T-3/CA decreased with the increase of the initial concentration of MO. At a lower initial concentration of MO, fiber membranes CS/CA and C-T-3/CA provided sufficient reactive sites for removal of MO. With the increase of initial concentration of MO, the total amount of MO molecules increased. However, the amount of fiber membranes remained unchanged, meaning that the amount of reactive sites did not change. Therefore, the removal ratio of MO decreased at the higher initial concentration of MO. C-T-3/CA showed a higher removal ratio of 98.4% than CS/CA at initial concentration of 10 mg/L due to simultaneous adsorption and photocatalysis for the MO removal by C-T-3/CA.

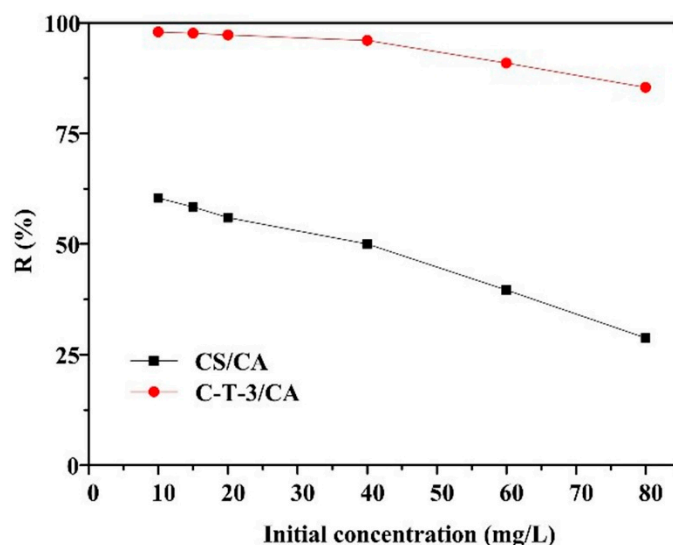


Figure 8. Effect of initial concentration on the MO removal amount.

3.3.4. Effect of Contact Time and Kinetic Study

The effect of time on the removal capacity of MO by CS/CA and C-T-3/CA are shown in Figure 9a. As time increased, the removal amount of MO by CS/CA and C-T-3/CA increased and then gradually reached the equilibrium state. In the initial stage ($t < 25$ min), due to the large number of active sites in both adsorbents, the removal amount of MO increased rapidly with the increase of contact time. The removal amount of MO increased slowly and finally reached the equilibrium 25 min later [49]. For CS/CA, the adsorption equilibrium appeared at 40 min, while for C-T-3/CA, equilibrium was reached at 60 min. Due to the addition of TiO_2 nanoparticles, which increased the specific surface area of the fiber membrane, more time was taken for the MO to penetrate the fiber membranes. Therefore, the contact time of 60 min was used for subsequent tests to ensure sufficient adsorption and photocatalytic degradation treatment. The pseudo-first-order and pseudo-second-order kinetic models were used to study the behavior of MO removal of fiber membranes [46], which can be expressed as follows:

Pseudo-first-order kinetic model:

$$\log(q_e - q_t) = \log q_e - \frac{k_1}{2.303} t \quad (3)$$

Pseudo-second-order kinetic model:

$$\frac{t}{q_t} = \frac{1}{k_2 q_e^2} + \frac{t}{q_e} \quad (4)$$

where q_e and q_t (mg/g) represent the equilibrium removal amount and the removal amount at time t ; k_1 and k_2 are the constants pseudo-first-order and pseudo-second-order rate, respectively.

The experimental kinetic curves of MO removal are shown in Figure 9b,c. The relevant kinetic parameters calculated from the curves are listed in Table 2. The correlation coefficients of the pseudo-first-order model and the pseudo-second-order model for MO removal by CS/CA were nearly equal to and greater than 0.95, indicating that physical adsorption and chemical adsorption all contributed to the removal of MO. The R^2 of the pseudo-second-order model (0.9952) was higher than that of the pseudo-first-order model (0.9878) for the removal of MO by C-T-3/CA. This suggested that fiber membranes exhibited mainly chemical adsorption accompanied by physical adsorption via the addition of TiO_2 [50].

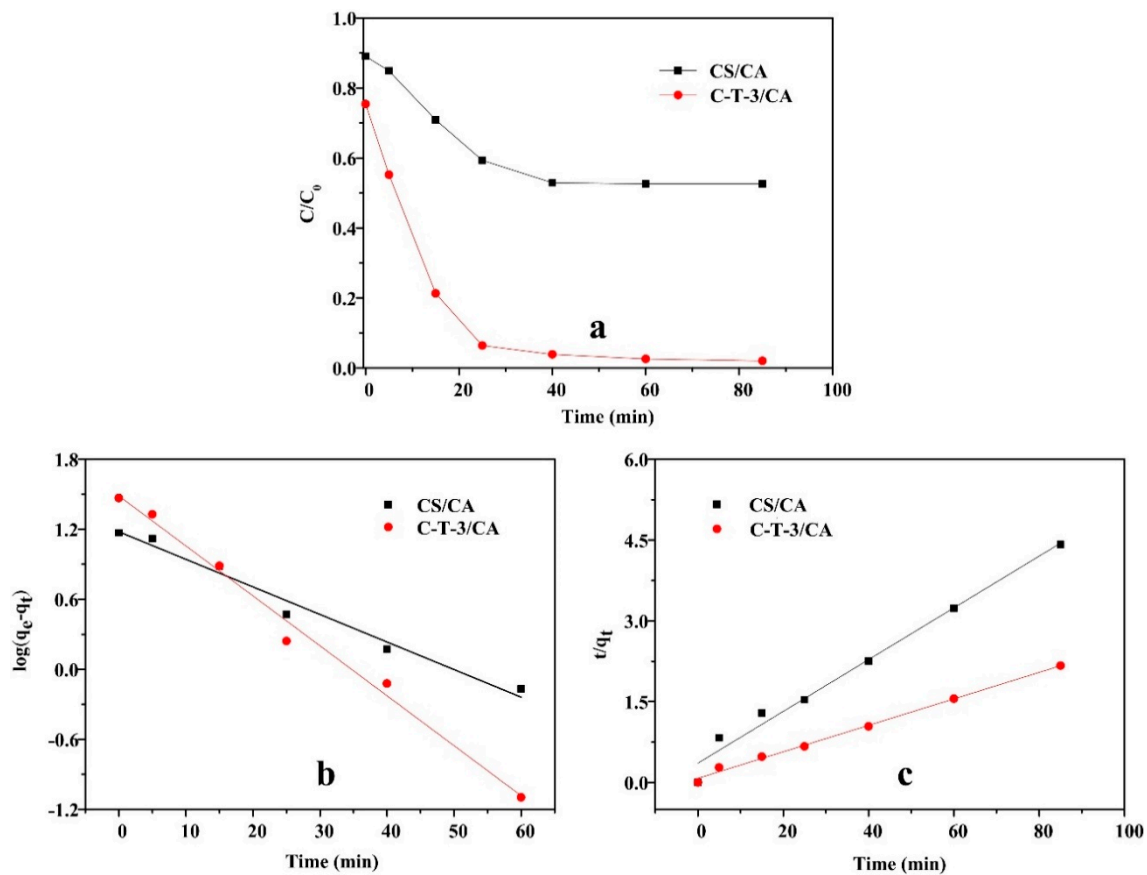


Figure 9. Effect of contact time on the MO removal amount. (a) The kinetics model for MO removal, (b) pseudo-first-order model, and (c) pseudo-second-order model.

Table 2. Kinetics parameters for MO removal.

Sample	$q_{e, exp}$ (mg/g)	Pseudo-First-Order Model			Pseudo-Second-Order Model		
		k_1	R^2	$q_{e, cal}$ (mg/g)	k_2	R^2	$q_{e, cal}$ (mg/g)
CS/CA	19.24	5.44×10^{-2}	0.9748	15.08	13.48×10^{-2}	0.9799	20.80
C-T-3/CA	39.20	9.86×10^{-2}	0.9878	30.61	32.33×10^{-2}	0.9952	40.67

3.3.5. Isotherm Study

The Langmuir model and Freundlich model were used to describe the isotherm equilibrium data of MO removal by CS/CA and C-T-3/CA fiber membranes [50]. It can be expressed as Equations (5) and (6)

The Langmuir model:

$$\frac{C_e}{q_e} = \frac{1}{q_m K_L} + \frac{C_e}{q_m} \tag{5}$$

The Freundlich model:

$$\log q_e = \frac{1}{n} \log C_e + \log K_F \tag{6}$$

where q_e (mg/g) represents the equilibrium removal amount, C_e (mg/L) is the equilibrium concentration of MO in aqueous solution and q_m (mg/g) represents the maximum removal amount, K_L is the Langmuir isotherm constant related to free energy and K_F and n are the Freundlich isotherm constant which expressed removal capacity and removal intensity, respectively.

The experimental isotherm curves of MO removal are shown in Figure 10a,b. The relevant isotherm parameters calculated from the curves are listed in Table 3. On the basis of the correlation coefficients of MO removal by CS/CA, the Freundlich isotherm model (Figure 9b) was better fitted than the Langmuir isotherm model (Figure 9a). Therefore, the CS/CA mainly exhibited multiple layers of adsorption. After the addition of TiO₂, the correlation coefficients of the Langmuir model and Freundlich model were approximately equal, indicating that C-T-3/CA exhibited multiadsorption behavior. This might be due to both the effects of photocatalytic degradation and adsorption [50].

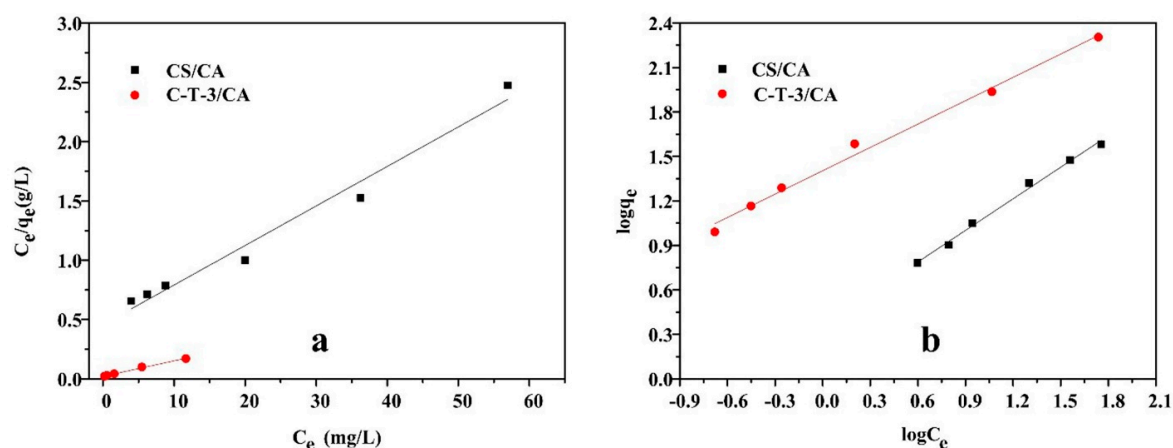


Figure 10. Isotherm model of MO removal: (a) Langmuir model, (b) Freundlich model.

Table 3. Isotherm parameters for MO removal.

Sample	Langmuir Model			Freundlich Model		
	K_L	q_m (mg/g)	R^2	K_F	n	R^2
CS/CA	7.28×10^{-2}	30.01	0.9714	2.30	1.41	0.9932
C-T-3/CA	62.5×10^{-2}	76.22	0.9948	25.33	1.90	0.9997

3.4. Removal Mechanism Analysis

3.4.1. FTIR Spectra Results

The FTIR spectra of C-T-3/CA fibers before and after removal of MO are demonstrated in Figure 11. Before removal of MO, the peaks at 3100–3500 cm^{-1} were ascribed to $-\text{OH}$ and $-\text{NH}_2$, 1638 and 1572 cm^{-1} were attributed to $-\text{NH}_3^+$ and $-\text{NH}_2$ of CA and CS, respectively. The peak appearing at 1154 cm^{-1} was attributed to the stretching of the C–O–C band of CA. The peaks in the range of 400–800 cm^{-1} were ascribed to the characteristic absorption of Ti–O [47,51]. After the adsorption and photocatalytic degradation of MO, the peak of the $-\text{NH}_2$ group at 1572 cm^{-1} decreased and the $-\text{NH}_3^+$ at 1638 cm^{-1} increased [49]. It demonstrated that $-\text{NH}_2$ was protonated as $-\text{NH}_3^+$ in the process of MO removal. Several new characteristic peaks that appeared were listed as follows: 1400–1450 cm^{-1} were ascribed to $-\text{N}=\text{N}-$ group, and 1039 cm^{-1} was attributed to $-\text{SO}_3^-$ of MO. It showed that MO was adsorbed on surfaces of CS molecules during the reaction process. The peaks at 3100–3500 cm^{-1} increased, which might be due to the formation of abundant active hydroxyl radicals ($\cdot\text{OH}$) during the photodegradation process (see Equations (9) and (10)).

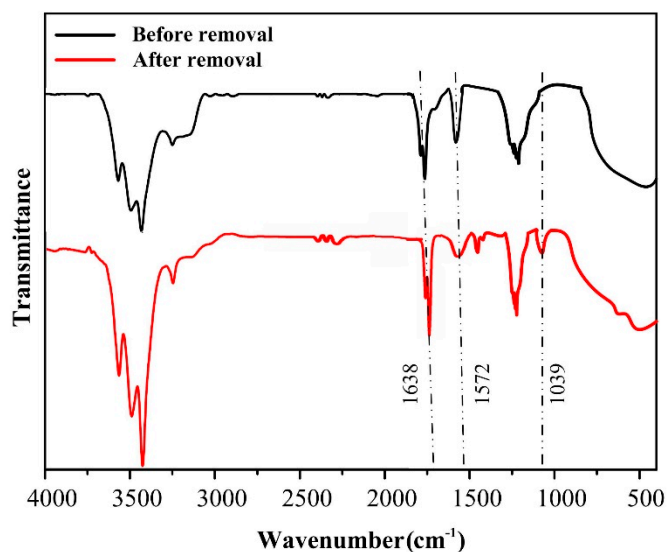


Figure 11. FTIR spectra of C-T-3/CA before and after MO removal.

3.4.2. XPS Spectra Results

As shown in Figure 12, XPS was employed to analyze the chemical element of the membrane surface before and after the removal (that allowed for coinstantaneous adsorption and photocatalysis) of MO with full-range and magnified spectra of S, N, O and Ti. It can be seen in Figure 12a that C-T-3/CA membranes before MO removal showed peaks of binding energy at 285.5, 397.7, 531.2 and 457.1 eV, which were assigned to carbon atom (C 1s), oxygen atom (O 1s), nitrogen atom (N 1s) and titanium atom (Ti 2p), respectively. As seen in Figure 12b, the peak of S 2p appeared at 167.7 eV after removal of MO, indicating MO adsorbed on the surface fiber membranes. For the N 1s spectrum in Figure 12c, the peak at 399.1 eV was assigned to $-\text{NH}_2$ group before MO removal. After MO removal, a new peak appeared at 401.7 eV and was attributed to $-\text{NH}_3^+$, and the peak of $-\text{NH}_2$ at 399.1 eV shifted to 399.8 eV. This indicated that $-\text{NH}_2$ was protonated as $-\text{NH}_3^+$, and electron transfer occurred between $-\text{NH}_2$ and MO molecules, respectively [22]. As seen in Figure 12d,e, the O 1s and Ti 2p binding energy increased after the removal of MO. Ti could exist in the form of TiOH_2^+ in acid solutions. After the reaction with MO molecules, the groups of $-\text{OH}_2^+$ as electron acceptors could interact with $-\text{SO}_3^-$ of MO due to electrostatic attraction, which could influence charge density of Ti and O [20].

3.4.3. BET Analysis

The BET results of CS/CA and C-T-3/CA membranes were measured by nitrogen adsorption method (see Table 4). After the addition of TiO_2 , the fiber membrane attained higher specific surface area and pore volume owing to uniform distribution of TiO_2 on CS hemispheres and an increase of the distance among C-T hemispheres (see Figure 3d). Therefore, the relative high adsorption capacity of MO on C-T-3/CA was ascribed to the high specific surface area, which should be good for the photodegradation of MO.

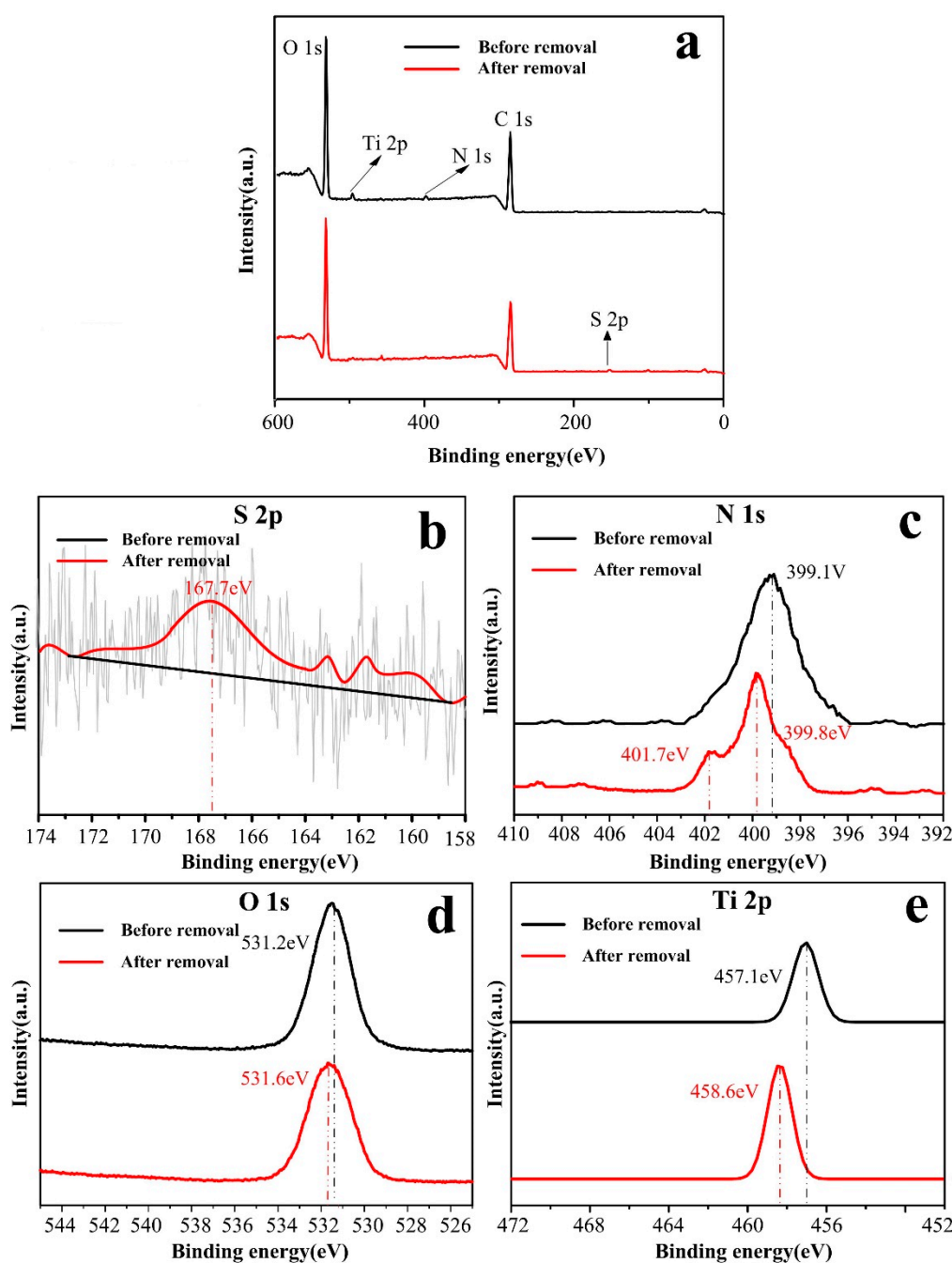


Figure 12. XPS spectra of C-T-3/CA before and after MO removal.

Table 4. BET results of CS/CA and C-T-3/CA.

Sample	Specific Surface Area (m ² /g)	Pore Volume (cc/g)	Average Pore Diameter (nm)
CS/CA	301.30	0.33	4.39
C-T-3/CA	342.10	0.48	4.79

3.4.4. Mechanism Analysis

According to the above analysis, the high removal capacity of C-T-3/CA was mainly due to the effective dispersion of TiO₂ in combination with CS, which improved the specific surface area of fiber membranes and increased the sites of photocatalytic degradation and adsorption. MO molecules could be adsorbed to the vicinity of photodegradation sites by electrostatic attraction between CS and

MO molecules, promoting the contact probability of TiO₂ and MO in the following photocatalytic degradation process. The reaction mechanism between MO and C-T-3/CA is illustrated in Figure 13. The mechanism of photocatalysis is summarized from Equation (7) to Equation (12). The MO removal mechanism included: (1) Adsorption, the electrostatic attraction between –NH₃⁺ group of CS and –SO₃[−] of MO molecules; (2) photocatalysis, the photocatalytic degradation of the MO by UV illumination began with photoexcitation of the TiO₂ and then formed an electron-hole pair (Equation (7)). High oxidation valence-band holes (h⁺) directly oxidized MO degradation (Equation (8)). Water decomposition produced ·OH (Equation (9)) or a reaction of h⁺ with OH[−] (Equation (10)). Meanwhile, the reaction between conduction-band electrons (e[−]) and proper electron acceptors (such as O₂) yielded oxidative radicals as described by Equation (11). The generated hydroxyl radicals easily degraded MO to form inorganic small molecules (Equation (12)) [6]. These results agreed with BET, FTIR and XPS analyses.

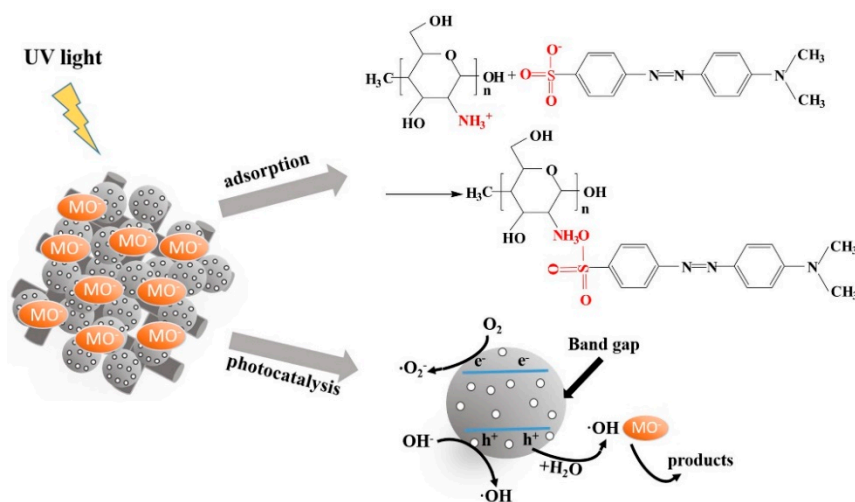


Figure 13. The mechanism of MO removal by C-T-3/CA.

3.5. Recycling Ability

To research the recycling ability of the composite membranes, the absorbance changes were measured in five cycles of MO removal. As demonstrated in Figure 14, the MO removal of fiber membranes was almost invariable for five consecutive cycles. The membranes still had a removal ratio of 98% at the end of the fifth cycle, testifying that the membranes maintained good performance of adsorption and photocatalytic degradation. This was because the stability of CS in aqueous solutions was improved by the intermolecular hydrogen bonds between CS and CA, and TiO₂ could be uniformly distributed via the interactions with CS molecules for effective photocatalytic degradation of MO [45].

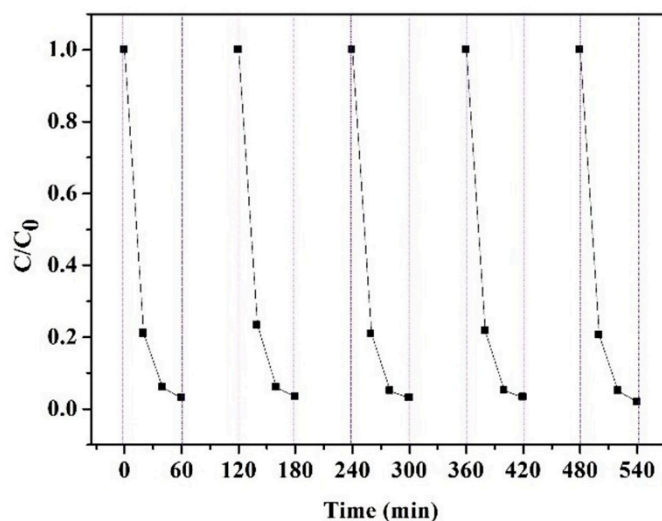


Figure 14. MO removal by C-T-3/CA in five cycles.

4. Conclusions

In this work, the C-T/CA fiber membranes were prepared via electrospinning and electrospraying. After the addition of TiO₂, the removal capacity of MO was improved, as a result of concurrent adsorption and photocatalytic degradation. When TiO₂ content was 3 wt %, the highest MO removal amount for fiber membranes (C-T-3/CA) was reached, 98% at pH value of 4 and MO concentration of 40 mg/L. The kinetic and isotherm model for the removal of MO by fiber membranes were well fitted pseudo-second-order kinetic and Freundlich isotherm models. Especially, C-T-3/CA membranes exhibited multiple layer adsorption with the addition of TiO₂. The involved mechanisms including adsorption and photocatalytic reaction occurred in the removal process which was demonstrated by FTIR, XPS and BET results. The recycling experiment showed fiber membrane had excellent stability and reusability.

Author Contributions: Conceptualization and methodology, X.S. and L.L.; investigation, X.S. and X.Z.; formal analysis and validation, X.S. and L.M.; writing—original draft preparation, X.S.; writing—review and editing, all the authors; funding acquisition, C.X. and L.L.

Funding: This research was funded by the National Natural Science Foundation of China (No. 51103058).

Acknowledgments: The authors acknowledge Jingya Wang for absorbance detection.

Conflicts of Interest: The authors declare no conflict of interest.

References

1. Cantarella, M.; Sanza, R.; Buccheria, M.A.; Ruffino, F.; Rappazzo, G.; Scalesed, S.; Impellizzeri, G.; Romano, L.; Privitera, V. Immobilization of nanomaterials in PMMA composites for photocatalytic removal of dyes, phenols and bacteria from water. *J. Photochem. Photobiol. Chem. A* **2016**, *321*, 1–11. [[CrossRef](#)]
2. Zhang, Y.F.; Park, M.; Kim, H.Y.; Newehy, M.E.; Rhee, K.Y.; Park, S.J. Effect of TiO₂ on photocatalytic activity of polyvinylpyrrolidone fabricated via electrospinning. *Compos. Part B Eng.* **2015**, *80*, 355–360. [[CrossRef](#)]
3. Pahasupanan, T.; Suwannahong, K.; Dechaphanya, W.; Rangkupan, R. Fabrication and photocatalytic activity of TiO₂ composite membranes via simultaneous electrospinning and electrospraying process. *J. Environ. Sci.* **2018**, *72*, 13–24. [[CrossRef](#)] [[PubMed](#)]
4. Doh, S.J.; Kim, C.; Lee, S.G.; Lee, S.J.; Kim, H. Development of photocatalytic TiO₂ fibers by electrospinning and its application to degradation of dye pollutants. *J. Hazard. Mater.* **2008**, *154*, 118–127. [[CrossRef](#)] [[PubMed](#)]
5. Odling, G.; Robertson, N. SILAR BiOI-Sensitized TiO₂ Films for Visible-Light Photocatalytic Degradation of Rhodamine B and 4-Chlorophenol. *Chem. Phys. Chem.* **2017**, *18*, 728–735. [[CrossRef](#)] [[PubMed](#)]

6. Ramos, P.G.; Flores, E.; Sánchez, L.A.; Candal, R.J.; Hojamberdiev, M.; Estrada, W.; Rodriguez, J. Enhanced photoelectrochemical performance and photocatalytic activity of ZnO/TiO₂ nanostructures fabricated by an electrostatically modified electrospinning. *Appl. Surf. Sci.* **2017**, *426*, 844–851. [[CrossRef](#)]
7. Du, P.F.; Song, L.X.; Xiong, J.; Cao, H.B. Photocatalytic degradation of Rhodamine B using electrospun TiO₂ and ZnO fibers: A comparative study. *J. Mater. Sci.* **2013**, *48*, 8386–8392. [[CrossRef](#)]
8. Song, J.; Wang, X.Q.; Yan, J.H.; Yu, J.Y.; Sun, G.; Ding, B. Soft Zr-doped TiO₂ Nanofibrous Membranes with Enhanced Photocatalytic Activity for Water Purification. *Sci. Rep.* **2017**, *7*, 1636. [[CrossRef](#)]
9. Zhang, J.; Hou, X.B.; Pang, Z.Y.; Cai, Y.B.; Zhou, H.M.; Lv, P.F.; Wei, Q.F. Fabrication of hierarchical TiO₂ fibers by microemulsion electrospinning for photocatalysis applications. *Ceram. Int.* **2017**, *43*, 15911–15917. [[CrossRef](#)]
10. Meichtry, J.M.; Levy, I.K.; Mohamed, H.H.; Dillert, R.; Bahnemann, D.W.; Litter, M.I. Mechanistic Features of TiO₂–Heterogeneous Photocatalysis of Arsenic and Uranyl Nitrate in Aqueous Suspensions Studied by the Stopped Flow Technique. *Chem. Phys. Chem.* **2016**, *17*, 885–892. [[CrossRef](#)]
11. Zhao, R.; Wang, Y.; Li, X.; Sun, B.L.; Wang, C. Synthesis of β -Cyclodextrin-Based Electrospun Nanofiber Membranes for Highly Efficient Adsorption and Separation of Methylene Blue. *ACS Appl. Mater. Interfaces* **2015**, *7*, 26649–26657. [[CrossRef](#)] [[PubMed](#)]
12. Yu, R.M.; Shi, Y.Z.; Yang, D.Z.; Liu, Y.X.; Qu, J.; Yu, Z.Z. Graphene oxide/chitosan aerogel microspheres with honeycomb-cobweb and radially oriented microchannel structures for broad-spectrum and rapid adsorption of water contaminants. *ACS Appl. Mater. Interfaces* **2017**, *9*, 21809–21819. [[CrossRef](#)] [[PubMed](#)]
13. Wei, L.J.; Zhang, H.M.; Cao, J. Electrospinning of Ag/ZnWO₄/WO₃ composite fibers with high visible light photocatalytic activity. *Mater. Lett.* **2019**, *236*, 171–174. [[CrossRef](#)]
14. Wang, C.H.; Shao, C.L.; Wang, L.J.; Zhang, L.N.; Li, X.H.; Liu, Y.C. Electrospinning preparation, characterization and photocatalytic properties of Bi₂O₃ fibers. *J. Colloid Interface Sci.* **2009**, *333*, 242–248. [[CrossRef](#)] [[PubMed](#)]
15. Jiang, J.H.; Liu, K.L.; Fan, W.Q.; Li, M.; Liu, Y.; Mao, B.D.; Bai, H.Y.; Shen, H.Q.; Yuan, S.L.; Shi, W.D. Electrospinning synthesis and photocatalytic property of Fe₂O₃/MgFe₂O₄ heterostructure for photocatalytic degradation of tetracycline. *Mater. Lett.* **2016**, *176*, 1–4.
16. Mantilaka, M.P.; De Silva, R.T.; Ratnayake, S.P.; Amaratunga, G.; de Silva, K.N. Photocatalytic activity of electrospun MgO nanofibres: Synthesis, characterization and applications. *Mater. Res. Bull.* **2018**, *99*, 204–210. [[CrossRef](#)]
17. Wang, L.; Yang, G.R.; Peng, S.J.; Wang, J.N.; Ji, D.X.; Yan, W.; Ramakrishna, S. Fabrication of MgTiO₃ fibers by electrospinning and their photocatalytic water splitting activity. *Int. J. Hydrog. Energy* **2017**, *42*, 25882–25890. [[CrossRef](#)]
18. Li, Y.; Zhao, H.; Yang, M. TiO₂ nanoparticles supported on PMMA fibers for photocatalytic degradation of methyl orange. *J. Colloid Interface Sci.* **2017**, *508*, 500–507. [[CrossRef](#)]
19. Lv, C.D.; Sun, J.X.; Chen, G.; Zhou, Y.S.; Li, D.Y.; Wang, Z.K.; Zhao, B.R. Organic salt induced electrospinning gradient effect: Achievement of BiVO₄ nanotubes with promoted photocatalytic performance. *Appl. Catal. B Environ.* **2017**, *208*, 14–21. [[CrossRef](#)]
20. Huang, M.T.; Tu, H.; Chen, J.J.; Liu, R.; Liang, Z.Y.; Jiang, L.B.; Shi, X.W.; Du, Y.M.; Deng, H.B. Chitosan-rectorite microspheres embedded aminated polyacrylonitrile fibers via shoulder-to-shoulder electrospinning and electrospraying for enhanced heavy metal removal. *Appl. Surf. Sci.* **2018**, *437*, 294–303. [[CrossRef](#)]
21. Haider, S.; Park, S.Y. Preparation of the electrospun chitosan nanofibers and their applications to the adsorption of Cu (II) and Pb (II) ions from an aqueous solution. *J. Membrane Sci.* **2009**, *328*, 90–96. [[CrossRef](#)]
22. Xin, S.J.; Zeng, Z.Y.; Zhou, X.; Luo, W.J.; Shi, X.W.; Wang, Q.; Deng, H.B.; Du, Y.M. Recyclable *Saccharomyces cerevisiae* loaded nanofibrous mats with sandwich structure constructing via bio-electrospraying for heavy metal removal. *J. Hazard. Mater.* **2017**, *324*, 365–372. [[CrossRef](#)]
23. Lee, C.G.; Javed, H.; Zhang, D.N.; Kim, J.H.; Westerhoff, P.; Li, Q.L.; Alvarez, P.J.J. Porous electrospun fibers embedding TiO₂ for adsorption and photocatalytic degradation of water pollutants. *Environ. Sci. Technol.* **2018**, *52*, 4285–4293. [[CrossRef](#)]
24. Malik, R.; Tomer, V.K.; Joshi, N.; Dankwort, T.; Lin, L.W.; Kienle, L. Au-TiO₂-Loaded Cubic g-C₃N₄ Nanohybrids for Photocatalytic and Volatile Organic Amine Sensing Applications. *ACS Appl. Mater. Interfaces* **2018**, *10*, 34087–34097. [[CrossRef](#)]

25. Gonzalez, P.A.; Bercero, M.Á.L.; Barrientos, L.; Valenzuela, M.L.; Díaz, C. Solid State Tuning of TiO₂ Morphology, Crystal Phase and Size through Metal Macromolecular Complexes and its significance in the Photocatalytic Response. *ACS Appl. Energy Mater.* **2018**, *1*, 3159–3170. [[CrossRef](#)]
26. Nasr, M.; Balme, S.; Eid, C.; Habchi, R.; Miele, P.; Bechelany, M. Enhanced Visible–Light Photocatalytic Performance of Electrospun GO/TiO₂ Composite Fibers. *J. Phys. Chem. C* **2017**, *121*, 261–269. [[CrossRef](#)]
27. Chung, L.; Chen, W.F.; Koshy, P.; Sorrell, C.C. Effect of Ce–doping on the photocatalytic performance of TiO₂ thin films. *Mater. Chem. Phys.* **2017**, *197*, 236–239. [[CrossRef](#)]
28. Seong, D.B.; Son, Y.R.; Park, S.J. A study of reduced graphene oxide/leaf–shaped TiO₂, fibers for enhanced photocatalytic performance via electrospinning. *J. Solid State Chem.* **2018**, *266*, 196–204. [[CrossRef](#)]
29. Zhang, J.; Cai, Y.B.; Hou, X.B.; Zhou, H.M.; Qiao, H.; Wei, Q.F. Preparation of TiO₂ Nanofibrous Membranes with Hierarchical Porosity for Efficient Photocatalytic Degradation. *J. Phys. Chem. C* **2018**, *122*, 8946–8953. [[CrossRef](#)]
30. Deng, L.G.; Taxipalati, M.; Zhang, A.; Que, F.; Wei, H.W.; Feng, F.Q.; Zhang, H. Electrospun chitosan/polyethylene oxide/lauric arginate nanofibrous film with enhanced antimicrobial activity. *J. Agric. Food Chem.* **2018**, *66*, 6219–6226. [[CrossRef](#)]
31. Xu, T.; Yang, H.Y.; Yang, D.Z.; Yu, Z.Z. Polylactic Acid Nanofiber Scaffold Decorated with Chitosan Islandlike Topography for Bone Tissue Engineering. *ACS Appl. Mater. Interfaces* **2017**, *9*, 21094–21104. [[CrossRef](#)]
32. Liu, H.; Wen, W.; Chen, S.T.; Zhou, C.G.; Luo, B.H. Preparation of Icarin and Deferoxamine Functionalized Poly(L–lactide)/chitosan Micro/Nanofibrous Membranes with Synergistic Enhanced Osteogenesis and Angiogenesis. *ACS Appl. Bio Mater.* **2018**, *1*, 389–402. [[CrossRef](#)]
33. Severyukhina, A.N.; Parakhonskiy, B.V.; Prikhozhenko, E.S.; Gorin, D.A.; Sukhorukov, G.B.; Möhwald, H.; Nanoplasmonic, A.M.Y. Chitosan Fibers as Effective SERS Substrate for Detection of Small Molecules. *ACS Appl. Mater. Interfaces* **2015**, *7*, 15466–15473. [[CrossRef](#)]
34. Tian, L.D.; He, X.W.; Lei, X.F.; Qiao, M.T.; Gu, J.W.; Zhang, Q.Y. An efficient and green fabrication of porous magnetic chitosan particles based on high adhesive superhydrophobic polyimide fiber mat. *ACS Sustain. Chem. Eng.* **2018**, *6*, 12194–12924. [[CrossRef](#)]
35. Li, Z.Y.; Li, T.T.; An, L.B.; Fu, P.F.; Gao, C.J.; Zhang, Z.M. Highly efficient chromium (VI) adsorption with nanofibrous filter paper prepared through electrospinning chitosan/polymethylmethacrylate composite. *Carbohydr. Polym.* **2016**, *137*, 119–126. [[CrossRef](#)]
36. Li, L.; Li, Y.X.; Cao, L.X.; Yang, C.F. Enhanced chromium (VI) adsorption using nanosized chitosan fibers tailored by electrospinning. *Carbohydr. Polym.* **2015**, *125*, 206–213. [[CrossRef](#)]
37. Li, C.Y.; Lou, T.; Yan, X.; Long, Y.Z.; Cui, G.P.; Wang, X.J. Fabrication of pure chitosan nanofibrous membranes as effective. *Int. J. Biol. Macromol.* **2018**, *106*, 768–774. [[CrossRef](#)]
38. Huang, P.; Xia, D.; Kazlaucinas, A.; Thornton, P.; Lin, L.; Menzel, R. Dye–Mediated Interactions in Chitosan–Based Polyelectrolyte/Organoclay Hybrids for Enhanced Adsorption of Industrial Dyes. *ACS Appl. Mater. Interfaces* **2019**, *11*, 11961–11969. [[CrossRef](#)]
39. Rodríguez, K.; Rennekar, S.; Gatenholm, P. Biomimetic Calcium Phosphate Crystal Mineralization on Electrospun Cellulose–Based Scaffolds. *ACS Appl. Mater. Interfaces* **2011**, *3*, 681–689. [[CrossRef](#)]
40. Arslan, O.; Aytac, Z.; Uyar, T. Superhydrophobic, Hybrid, Electrospun Cellulose Acetate Nanofibrous Mats for Oil/Water Separation by Tailored Surface Modification. *ACS Appl. Mater. Interfaces* **2016**, *8*, 19747–19754. [[CrossRef](#)]
41. Liu, L.; He, D.; Wang, G.S.; Yu, S.H. Bioinspired Crystallization of CaCO₃ Coatings on Electrospun Cellulose Acetate Fiber Scaffolds and Corresponding CaCO₃ Microtube Networks. *Langmuir* **2011**, *27*, 7199–7206. [[CrossRef](#)]
42. Zhang, G.; Sun, M.; Liu, Y.; Liu, H.J.; Qu, J.H.; Li, J.H. Ionic Liquid Assisted Electrospun Cellulose Acetate Fibers for Aqueous Removal of Triclosan. *Langmuir* **2015**, *31*, 1820–1827. [[CrossRef](#)]
43. Wang, L.H.; Yang, H.; Hou, J.Z.; Zhang, W.X.; Xiang, C.H.; Li, L.L. Effect of the electrical conductivity of core solutions on the morphology and structure of core–shell CA–PCL/CS fibers. *New J. Chem.* **2017**, *41*, 15072–15078. [[CrossRef](#)]
44. Salihu, G.; Goswami, P. Hybrid electrospun nonwovens from chitosan/cellulose acetate. *Cellulose* **2012**, *19*, 739–749. [[CrossRef](#)]

45. Peng, L.C.; Li, H.; Meng, Y.H. Layer-by-layer structured polysaccharides-based multilayers on cellulose acetate membrane: Towards better hemocompatibility, antibacterial and antioxidant activities. *Appl. Surf. Sci.* **2017**, *401*, 25–39. [[CrossRef](#)]
46. Razzaz, A.; Ghorban, S.; Hosayni, L.; Irani, M.; Aliabadi, M. Chitosan nanofibers functionalized by TiO₂ nanoparticles for the removal of heavy metal ions. *J. Taiwan Inst. Chem. Eng.* **2016**, *58*, 333–343. [[CrossRef](#)]
47. Yousefi, B.; Charehaghaji, A.A.; Jeddi, A.A.A.; Karimi, M. The Combined Effect of Wrinkles and Noncircular Shape of Fibers on Wetting Behavior of Electrospun Cellulose Acetate Membranes. *J. Polym. Sci. B* **2018**, *56*, 1012–1020. [[CrossRef](#)]
48. Gebru, K.A.; Das, C. Removal of Pb (II) and Cu (II) ions from wastewater using composite electrospun cellulose acetate/titanium oxide (TiO₂) adsorbent. *J. Water Process Eng.* **2017**, *16*, 1–13. [[CrossRef](#)]
49. Ranjbari, S.; Tanhaei, B.; Ayati, A.; Sillanp, M. Novel Aliquat-336 impregnated chitosan beads for the adsorptive removal of anionic azo dyes. *Int. J. Biol. Macromol.* **2019**, *125*, 989–998. [[CrossRef](#)]
50. Wang, P.P.; Wang, L.H.; Dong, S.J.; Zhang, G.H.; Shi, X.J.; Xiang, C.H.; Li, L.L. Adsorption of hexavalent chromium by chitosan/poly(ethylene oxide)/permutit electrospun fibers. *New J. Chem.* **2018**, *42*, 17740–17749. [[CrossRef](#)]
51. Rahimi, K.; Mirzaei, R.; Akbari, A.; Mirghaffari, N. Preparation of nanoparticle-modified polymeric adsorbent using wastage fuzzes of mechanized carpet and its application in dye removal from aqueous solution. *J. Clean. Prod.* **2017**, *178*, 373–383. [[CrossRef](#)]



© 2019 by the authors. Licensee MDPI, Basel, Switzerland. This article is an open access article distributed under the terms and conditions of the Creative Commons Attribution (CC BY) license (<http://creativecommons.org/licenses/by/4.0/>).